

Heterogeneity governs diameter-dependent toughness and strength in SiC nanowires

Fazle Elahi, Ling Ma, and Zubaer M. Hossain*

Department of Mechanical Engineering, Laboratory of Mechanics & Physics of Heterogeneous Materials, University of Delaware, Newark, Delaware 19716, USA (Received 27 August 2018; revised manuscript received 9 November 2018; published 27 November 2018)

Using a combination of density functional theory and molecular dynamics simulations, this paper reveals the atomistic origin of diameter-dependent extreme mechanical behavior of [111] 3C-SiC nanowires obtained from an energy-based framework. Our results suggest that heterogeneity in atomic stress and variations in diameter-dependent potential-energy density have a profound impact on extreme mechanical properties in the nanowires. The heterogeneity in stress evolves from the nonuniform bond lengths mediated by low coordinated surface atoms—and it penetrates the entire cross section in thinner nanowires and constitutes the atomistic basis for their large reduction in fracture strain, toughness, and strength. Although stress heterogeneity is substantially higher in ultrathin nanowires, its intensity drops and saturates rapidly in larger nanowires following a nonlinear dependence on diameter. The maximum stress heterogeneity in a cross section localizes crack nucleation at the core in ultrathin nanowires but near the surface in larger nanowires. Moreover results show that stiffness, toughness, strength, and fracture strain of the nanowires increase nonlinearly with increasing diameter and saturate at a lower value compared to bulk SiC. In addition to resolving wide discrepancies in the reported values of the first-order elastic modulus in SiC nanowires, the findings highlight heterogeneity as a critical factor for inducing diameter-dependent extreme mechanical behavior in brittle nanowires.

DOI: [10.1103/PhysRevB.98.174111](https://doi.org/10.1103/PhysRevB.98.174111)**I. INTRODUCTION**

Strength and toughness are two crucial mechanical properties of a solid that dictate its ability to function reliably under extreme conditions. For brittle solids (such as SiC, Si, Ge, or SiO₂) the ideal strength is defined by the maximum stress and the toughness by the maximum elastic energy density that the solid can withstand prior to failure. These are well-defined intensive properties for a bulk solid, but they act like an extensive property in nanostructured solids due to the presence of surfaces which alter the energetics of the material and associated mechanical behavior [1–15].

Until recently, it was believed that the evolution of surface stress in nanowires (NWs) is the key factor for inducing a variety of diameter-dependent (*d*-dependent) mechanical and structural features in nanowires. Although a surface can set up various interconnected effects including surface stress [12], surface potential [13], surface energy [16], charge density [14], chemical reactions [17], and atomic reconstruction [15], it is generally surface stress that is used to explain various mechanisms in nanowires including self-healing, surface reorientation, phase transformation, yielding, failure, and ductile-to-brittle transition [1–11]. Recent findings nonetheless contradict several surface-stress-based explanations. For instance, softening or stiffening behavior of metallic nanowires is shown to be controlled by the orientation-dependent nonlinear elasticity at the core alone [18]. Also, instability to plastic shear has been shown experimentally to originate mainly from the surface energy

[19], which violates several surface-stress-based interpretations [11,20–22] that are mostly built upon the assumption of isotropy and homogeneity in material properties [12].

Additionally, substantial efforts have been devoted to predict the first-order elastic modulus in a range of nanowires [23–30]; but analogous efforts remain missing for the higher-order elastic properties of nanowires and their failure mechanisms that can reveal the atomistic processes responsible for the nucleation of defects causing catastrophic failure under practical conditions. Extreme mechanical properties of nanowires and their atomistic basis therefore continue to puzzle scientists and engineers, invoking novel insight and understanding on the subject [31,32].

Here, we focus on SiC nanowires which are brittle in character and have a variety of important applications in stretchable absorbers, fast-response ultraviolet detectors, pressure sensors, aerogels, biosensors, transistors, and reinforcements in composites due to high-temperature heat resistance, recoverability, chemical resistance, and lightweightness [33–37]. Silicon carbide has a number of polytypes, such as *a*-SiC, 6H-SiC, 4H-SiC, 2H-SiC, and 3C-SiC [37]. Among these polytypes, 3C-SiC nanowires have drawn wide attention due to their exceptional properties. Using *ab initio* simulations, it has been reported that 3C-SiC nanowires show remarkable *d*-dependent electronic properties with increased optical activity and electron mobility [27,38–41]. In the context of mechanical properties, it has been shown that the first-order elastic modulus depends strongly on diameter [29,41,42]. Nonetheless, the reported values cover a wide range of variations ranging from 150 to 700 GPa without any clear trend on its diameter-dependent behaviors [30]. The large discrepancy is attributed to several factors including: The way the diameter

*zubaer@udel.edu

is computed; applied boundary conditions (such as bending vs axial loading setup); and physical and experimental conditions of the nanowire [30]. In addition to inadequate information on diameter-dependent linear properties, the behavior of SiC NW in the nonlinear regime of mechanical deformation that governs higher-order elastic behavior and controls extreme mechanical properties, such as toughness and strength remain mostly unexplored.

Focusing on the [111] 3C-SiC nanowires (which have been proven to be the most energetically favorable surface orientation [43]), we demonstrate that force-based analysis of mechanical properties can suffer from ill-defined macroscopic geometric quantities, such as the volume or diameter of a nanowire. To address the limitations, we applied an energy-based framework and demonstrate it as a reliable alternative in assessing the mechanical behavior accurately. Our results suggest that diameter-dependent potential-energy density forms the basis of effective elastic properties in SiC NWs and their toughness, strength, and condition for crack nucleation are governed by the diameter-dependent stress heterogeneity. Our analysis is built upon two hypotheses: (i) higher potential-energy surfaces induce diameter-dependent heterogeneity in the stress fields of a nanowire that penetrate from its surface into the core, and (ii) bond deformation within the cross-sectional planes as well as along the longitudinal direction of a nanowire are nonuniform (despite equality in macroscopic strain), and this nonuniformity directly affects the nanoscopic mechanical state of nanowires.

In the following sections, we first outline our computational approach (in Sec. II) and then discuss the results on elastic and extreme properties of 3C-SiC nanowires (in Sec. III) from an atomistic viewpoint.

II. COMPUTATIONAL APPROACH

The most accurate mechanical behavior can be obtained from *ab initio* simulations based on density functional theory (DFT) [44]. It is, however, beyond the scope of DFT to capture the behavior of nanowires of wider cross sections due to large computational cost and the need for incorporating a large vacuum in the lateral directions to avoid the interactions between the periodic images of the nanowire. Moreover, incorporation of thermal effects in DFT-based molecular dynamics (MD) simulations of tensile deformation is highly computationally intensive and thus practically limited to modeling a few hundreds of atoms [45]. As an alternative classical molecular dynamics simulations can be performed and there are two potentials available: the Tersoff potential [46] and the Vashista potential [47]. They provide accurate behavior in the elastic regime but can exhibit a ductilelike pattern and unphysical stiffening of the lattice [48], which are inconsistent with the experimentally observed brittle fracture in 3C-SiC nanowires [28].

To address the limitations, we applied an integrated approach that uses a blend of DFT and MD simulations. The DFT simulation is used to obtain an accurate interatomic potential in the Stillinger-Weber (SW) form [49] for modeling both the elastic and the strength properties accurately, and the MD simulation is used to carry out deformation simulations for the nanowires of different diameters. Although we validate

the MD results for hydrostatic and uniaxial deformations of bulk SiC, for the nanowire results we limit the validation effort to a few computationally tractable nanowires due to limitations of the system size that can be dealt with DFT. The SW potential is selected due to its reliability in producing accurate elastic and extreme mechanical properties of brittle solids [50–52], simplicity in analytical form, ability to produce experimentally consistent brittlelike fracture surfaces, and small computational cost compared to the Tersoff or Vashishta potential.

A. Determining SW potential parameters

We determine the SW parameters following a strength-based mechanistic approach that has been successfully applied to model extreme properties of graphene [50,51] and hexagonal boron nitride [52]. This approach allows fitting equilibrium properties of the solid (such as force constant, lattice constant, and bending modulus) as well as its strength. In addition to reproducing the elastic properties near the equilibrium accurately, this strength-based approach reproduces the mechanical behavior of the material accurately over the entire deformation regime covering both the linear and the nonlinear regimes of mechanical deformation [50–52]. The detail methodology for obtaining the SW parameters from DFT is published elsewhere [50]; here, for completeness we mention the key steps of the procedure briefly.

In general, the SW potential models many-body interaction of a solid through a sum of two-body $V_2(r_{ij})$ and three-body $V_3(\theta_{ijk})$ interaction potentials where

$$V_2(r_{ij}) = A\epsilon \left(B \frac{\sigma^4}{r_{ij}^4} - 1 \right) \exp \left(\frac{\sigma}{r_{ij} - r_c} \right), \quad (1)$$

$$V_3(\theta_{ijk}) = \lambda\epsilon (\cos \theta_{ijk} - \cos \theta_0)^2 \exp \left(\frac{2\gamma\sigma}{r_{ij} - r_c} \right). \quad (2)$$

Here r_{ij} is the distance between atoms located at r_i and r_j ; θ_{ijk} is the angle between three atoms located at r_i , r_j , and r_k ; and A , B , ϵ , σ , λ , and γ are the SW parameters. The parameters A , B , σ , and λ are obtained from DFT-generated force-constant K_b , cohesive energy E_c , bond bending constant k_θ , and equilibrium bond length r_0 . Among the remaining parameters of the SW potential, we take r_c as the second-neighbor distance and exploit the free parameters γ and ϵ to calibrate the potential for accurate strength. Application of the above procedure results in the following SW parameters: $\epsilon = 1.9$, $\sigma = 2.1450$, $a = 1.42191$, $\lambda = 19.0$, $\gamma = 0.69000$, $\cos \theta = -0.33333$, $A = 11.79386$, $B = 0.27329$.

As demonstrated in Fig. 1, the potential provides an accurate description of mechanical behavior for bulk SiC over a wide range of uniaxial stress states spanning the linear and nonlinear regimes of mechanical deformation.

The DFT and MD results start deviating at around 12% strain—the deviation can be attributed to high-order many-body interactions that are taken into consideration in DFT but not in MD. Nevertheless all three mechanical properties (Young's modulus, ideal strength, and toughness) as well as fracture strain are well predicted by SW. The simulation

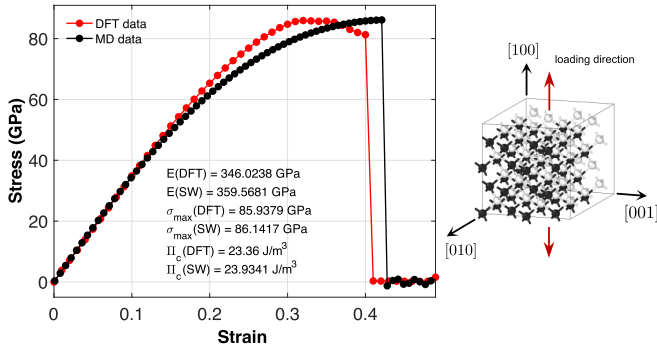


FIG. 1. Comparison of the stress-strain curves obtained from simulating uniaxial deformation of bulk 3C-SiC along the [100] direction using DFT-generalized gradient approximation (DFT-GGA) and MD-SW. Results on stiffness E , ideal strength σ_{\max} , and nucleation-toughness Π_c agree within 3.9%, 0.2%, and 1.5%, respectively. The simulation cell containing 96 atoms is displayed on the right.

details and boundary conditions are presented in the following section.

B. Simulation details

Our atomistic simulations involve both bulk and NW configurations. The nanowires are created from an assembly of cuboid unit cells with orthogonal sides described by the following lattice vectors:

$$\begin{aligned}
 a_1 &= 3[r_0 + (\sin \phi - \sqrt{2} \cos \phi)/4], \\
 a_2 &= 6(-\sin \phi \sin \theta + \cos \phi + \sin \phi \cos \theta)a/4,
 \end{aligned}$$

and

$$a_3 = (\sin \theta + \cos \theta)a/2.$$

Here $\theta = \pi/4$ and $\phi = \arctan \frac{1}{\sqrt{2}}$. There are 12 atoms in the orthorhombic unit cell of SiC. Their atomic coordinates are as follows: $\vec{r}_1 = (0, 0, r_0 + 2\delta_1)$, $\vec{r}_2 = (\delta_2, a_3/2, 0, 0)$, $\vec{r}_3 = (2\delta_2, 0, \delta_1)$, $\vec{r}_4 = (3\delta_2, a_3/2, 2\delta_1)$, $\vec{r}_5 = (4\delta_2, 0, 0)$, $\vec{r}_6 = (5\delta_2, a_3/2, \delta_1)$, $\vec{r}_7 = (0, 0, r_0 + 2\delta_1, 2r_0 + 2\delta_1)$, $\vec{r}_8 = (\delta_2, a_3/2, 0, 2r_0 + 3\delta_1)$, $\vec{r}_9 = (2\delta_2, 0, r_0 + \delta_1)$, $\vec{r}_{10} = (3\delta_2, a_3/2, 2r_0 + 2\delta_1)$, $\vec{r}_{11} = (4\delta_2, 0, 2r_0 + 3\delta_1)$, $\vec{r}_{12} = (5\delta_2, a_3/2, r_0 + \delta_1)$, where $\delta_1 = s_\phi a/4 - c_\phi a/(2\sqrt{2})$, $\delta_2 = (-s_\phi s_\theta + c_\phi + s_\phi c_\theta)a/4$, and $\delta_3 = (s_\theta + c_\theta)a/4$ are the interplanar spacing along the [111], [11 $\bar{2}$], and [$\bar{1}$ 10] directions, respectively, $r_0 = 1.905$ Å is the equilibrium bond length, and $a = 4.4015$ Å is the equilibrium lattice constant of our SiC-SW potential which agrees with the corresponding lattice parameter of 4.385 Å obtained from our DFT-GGA calculation and with the experimental value of 4.36 Å [27,53] within 1%. Figure 2 illustrates the unit cell with two orthographic projections and cross section of an example [111]-SiC nanowire.

The NW configurations are periodic along the [111] direction with an empty space in the lateral directions to allow Poisson's contraction. They are simulated with tetragonal supercell with its surface normals pointing along the [111], [11 $\bar{2}$], and [$\bar{1}$ 10] directions. The NW diameters range from 0.32 to 6.53 nm which are sufficient to cover the thinnest

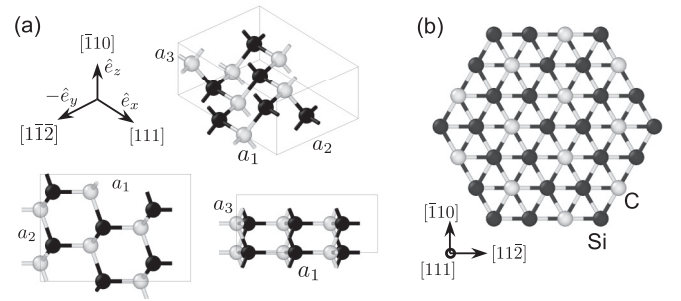


FIG. 2. (a) Twelve-atom unit cell of 3C-SiC with its two orthographic projections on the { $\bar{1}$ 10} and {11 $\bar{2}$ } planes. The loading direction is the [111] direction (aligned along the unit vector \hat{e}_x). (b) Cross-sectional view of a [111]-SiC nanowire of 0.98-nm diameter. Atoms are identified as Si and C.

possible nanowire and wide enough for drawing conclusive analysis on d -dependent mechanical behavior. We choose only hexagonal cross sections with side-length b which give the effective diameter $d = 1.81878b$. This d is used only to discuss the effective behavior of the NWs in terms of an effective geometric quantity, but it is not used in calculating stress for the reason stated in Sec. III A.

DFT simulation details. All of the DFT simulations are performed using the code SIESTA [54]. The core electrons are replaced by norm-conserving pseudopotentials following a Troullier and Martins scheme [55]. The valence electrons are represented by an extended numerical atomic basis set of polarized double- ζ type. For the exchange-correlation part of the electron energy we used the GGA with the Perdew-Burke-Ernzerhof functional [56]. The pseudopotentials (PPs) for Si and C were obtained from the SIESTA pseudopotential database. In generating the PPs the valence configuration used for Si was $3s^2, 3p^2, 3d^0$, and $4f^0$ with cutoff distances of 1.75, 1.94, 2.09, and 2.09 bohrs, respectively, for the pseudoatomic orbitals, whereas for C the valence configurations used were $2s^2, 2p^2, 3d^0$, and $4f^0$ with a cutoff at 1.54 bohrs. The energy shift used for the basis was 50 meV. For all the DFT calculations, an energy threshold of 1.0×10^{-4} eV per supercell and a force tolerance of 0.01 eV/Å were used to ensure convergence of the results. The relaxation of atoms and supercell was carried out by using the conjugate gradient optimizer with a maximum displacement of 0.05 Å at each relaxation step of the deformed configurations.

The DFT calculations involve simulations with two different bulk configurations (which we denote as B-1 and B-2 supercells) and five different nanowire configurations (which we denote as NW supercells). The B-1 supercell containing eight atoms and periodic in all directions is used to obtain the equilibrium structural parameters of the lattice (a_0 , k_b , and E_c) for use in developing the SW potential. In this calculation hydrostatic deformation is applied to the lattice for 100 different lattice constants (ranging from 3.4 to 12.0 Å). At each deformation state, only the atoms were allowed to relax keeping the volume of the supercell fixed. The Brillouin zone (BZ) integration was performed with a Monkhorst-Pack (MP) k mesh of $10 \times 10 \times 10$ that resulted in 560 k points in the reciprocal space of the domain. From the energy vs lattice constant data the equilibrium lattice constant is extracted as

$a_0 = 4.385 \text{ \AA}$ which agrees with the experimental value of 4.36 \AA [57] within 0.67%.

The B-2 supercell (containing 96 atoms and bounded by orthogonal sides with their surface normals along the [100], [010], and [001] directions in a $8.80967 \times 13.21451 \times 8.80967 \text{ \AA}^3$ periodic box) is used to determine the ideal strength of bulk SiC along the [100] direction. This strength value is used in calibrating the parameters (γ and λ) for the SW potential. In this DFT calculation, uniaxial stress deformation is applied along the [100] direction—and under the constraint of fixed dimension along the loading direction, the cell dimension along the [010] and [001] directions as well as the atoms are allowed to relax using the “volume cell optimization” scheme [54] (the corresponding stress-strain MD and DFT results were illustrated in Fig. 1). In this process a stress tolerance of 0.5 GPa was found to be sufficient to get convergence of the stress-tensor components. The BZ integration is conducted with a MP k mesh of $6 \times 4 \times 6$. Although the energy calculations were found to converge for a coarser mesh of $4 \times 2 \times 4$, the integration on a denser mesh was necessary to confirm convergence in each component of the stress tensor, particularly, at larger deformation.

The NW-supercell calculations involve uniaxial deformation simulation of nanowires. They are used to check the validity of the MD results on NWs. Due to large computational cost, these DFT-GGA simulations on NWs were limited to a maximum strain state of 10% for the five smallest nanowires containing 38, 74, 122, 182, and 254 atoms (with one unit cell along the [111] direction). The diameter of the nanowires ranges from 0.65 to 1.0 nm, and the 10% strain level is sufficient to calculate the first-order elastic modulus to validate the corresponding values obtained from MD. To avoid interactions between the periodic replicas of a nanowire along the $[11\bar{2}]$ and $[\bar{1}10]$ directions, an empty space of 10 \AA is considered on each side of the nanowire in the lateral directions—and at each deformation step, the atoms were relaxed keeping the cell-volume constant. For these calculations, we used a MP k mesh of $8 \times 1 \times 1$ where eight grid points were taken along the loading or periodic direction (along which the supercell contains only one unit cell).

MD simulation details. The MD simulations were performed using large-scale atomic/molecular assively parallel simulator (LAMMPS) [58] with the SW potential introduced in this paper. MD is used to obtain uniaxial stress-strain response of bulk SiC along the [100] direction (for the B-2 supercell) and for 20 NWs along the [111] direction.

Prior to applying deformation, the atomic system was relaxed using the conjugate gradient optimizer. During deformation of the B-2 supercell, the N - P - T ensemble [59] was used to allow Poisson contraction in the lateral directions. A pair of N6se-Hoover thermostats [60] and Anderson barostats [61,62] were applied to keep the temperature of the system at 1 K and pressure at 0 bars, respectively. To enable exploiting the periodic boundary condition along the loading direction and allow the Poisson contraction along the lateral directions under the isobaric condition in LAMMPS, the temperature was chosen to be 1 K. This low temperature essentially gives a static condition but yet allows using the LAMMPS MD setup. The static condition is needed to compare the MD results

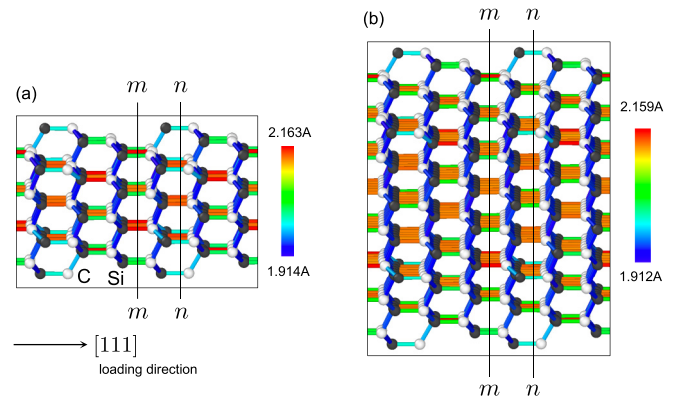


FIG. 3. Heterogeneity in bond lengths for (a) $d = 0.98 \text{ nm}$ and (b) $d = 1.96 \text{ nm}$ NWs at 15% macroscopic strain. The vertical lines mm and nn represent two cross-sectional planes at different locations along the loading direction highlighting nonuniformity in cross-sectional area and bond lengths. The atomic structures are rotated slightly with respect to the [111] direction to reveal heterogeneity in bond strain.

with those of DFT. The damping parameters used to control the thermostatic and barostatic effects were found to produce physically meaningful mechanical behavior for $\text{tdamp} = 1 \text{ ps}$ and $\text{pdamp} = 1 \text{ ps}$ with the time step of 1 fs. Here tdamp and pdamp are the parameter symbols used in LAMMPS. For the NW calculations with MD, ten unit cells were considered along the [111] direction. The cell dimensions along the lateral directions ($[11\bar{2}]$ and $[\bar{1}10]$) were kept fixed at each of the deformed state applied along the [111] direction at a strain rate of $1.0 \times 10^{-4} / \text{ps}$ (or $1.0 \times 10^8 / \text{s}$). An empty space of 20 \AA was introduced in the lateral directions to avoid interactions between the periodic images of the physical domain.

III. RESULTS AND DISCUSSIONS

A. Theoretical approach

In determining the elastic and extreme properties of nanowires, average stress needs to be calculated at different strain states in the linear and nonlinear regimes of mechanical deformation. Traditionally, this is performed by dividing the resultant force F acting on the supercell by the cross-sectional area A of the nanowire such that stress is defined as $\sigma = F/A$. This force-based approach is reliable when: (a) A is a well-defined quantity and constant throughout the nanowire along its axial direction, and (b) σ is uniform on A obeying the Saint-Venant’s (SV) principle [63–66]. For smaller nanowires, these conditions are easily violated as illustrated in Fig. 3 for two nanowires of diameters 0.98 and 1.96 nm.

It is evident that there are large variations in bond strain (thereby stress) at the given 15% macroscopic loading.

Although the bond deformation has some patterns following the repetition of the unit cell, there is a substantial variation in bond strain along the axial direction as well as across the nanowire section. The situation gets worse at finite temperatures because of the appearance of thermal fluctuations and phononic instability of the nanowires. Therefore, nonuniform bond deformation and associated variation in potential-energy density across the nanowire can make the stress fields highly

heterogeneous causing the force-based evaluation of mechanical properties violate the SV principle and susceptible to inaccuracies. Moreover owing to the ill conditioning of the effective diameter of nanowires, any macroscopic quantity (such as diameter or volume) that goes into predicting stress can potentially lead to spurious outcomes [30]. In some calculations reported in the literature, a new definition of radius has been proposed by adding first-order corrections [41]. Yet accurate computation of stress from force remains a nontrivial task for nanowires.

To address this challenge, we apply an energy-based approach that eliminates the use of diameter or a macroscopic geometric quantity in calculating stress thereby strength or toughness. Using nonlinear elasticity theory [67], elastic energy density of a solid can be written in terms of the strain components (up to the fifth order) as

$$u = C_{ijkl}\epsilon_{ij}\epsilon_{kl} + C_{ijklmn}\epsilon_{ij}\epsilon_{kl}\epsilon_{mn} + C_{ijklmnop}\epsilon_{ij}\epsilon_{kl}\epsilon_{mn}\epsilon_{op} + C_{ijklmnopqr}\epsilon_{ij}\epsilon_{kl}\epsilon_{mn}\epsilon_{op}\epsilon_{qr}, \quad (3)$$

where u is the elastic energy density (in the units of $\text{eV}/\text{\AA}^3$ per atom), ϵ_{ij} is the second-rank strain tensor, C_{ijkl} is the fourth-rank elasticity tensor, C_{ijklmn} is the sixth-rank elasticity tensor, $C_{ijklmnop}$ is the eighth-rank elasticity tensor, and $C_{ijklmnopqr}$ is the tenth-rank elasticity tensor. For uniaxial loading along the x direction, the above relation can be reduced to $u = C_{xxxx}\epsilon_{xx}^2 + C_{xxxxxx}\epsilon_{xx}^3 + C_{xxxxxxx}\epsilon_{xx}^4 + C_{xxxxxxx}\epsilon_{xx}^5$. Since each of the elasticity tensor components is a constant, we denote $C_{xxxx} = C_2$, $C_{xxxxxx} = C_3$, $C_{xxxxxxx} = C_4$, and $C_{xxxxxxx} = C_5$ to write u in a simple form

$$u = (C_2\epsilon_{xx}^2 + C_3\epsilon_{xx}^3 + C_4\epsilon_{xx}^4 + C_5\epsilon_{xx}^5). \quad (4)$$

Substituting $u = U/v_0$ in Eq. (4), where v_0 is the *effective atomic volume* and its units is in \AA^3 per atom. It arises from the transition from total energy of the solid to the energy density of elasticity theory. And U is the total elastic energy of the solid, we obtain

$$U = v_0(C_2\epsilon_{xx}^2 + C_3\epsilon_{xx}^3 + C_4\epsilon_{xx}^4 + C_5\epsilon_{xx}^5). \quad (5)$$

The constitutive relation can then be extracted by taking the first derivative of U with respect to ϵ_{xx} and taking the parameter v_0 as a constant and strain-independent quantity: $\sigma_{xx} = \frac{\partial U}{\partial \epsilon_{xx}}$. This results in the following constitutive relation:

$$\sigma_{xx} = v_0(2C_2\epsilon_{xx} + 3C_3\epsilon_{xx}^2 + 4C_4\epsilon_{xx}^3 + 5C_5\epsilon_{xx}^4). \quad (6)$$

Therefore, as long as the elastic energy density and stress state of the material have fifth-order and fourth-order dependences on strain, respectively, v_0 needs to be evaluated only once for a material. It should be noted that for a bulk material, both U and σ_{xx} are separately available from simulations. For NWs, on the other hand, the total energy is readily available but not the stress as the latter needs some conversion to account for the empty space. This can be avoided if v_0 is estimated from bulk simulations as described below.

Because the energy-based definition of stress stated above results in a fourth-order expression in ϵ_{xx} , we can consider fitting a similar polynomial to the atomistic stress-strain data obtained from bulk simulations. Let us denote that polynomial

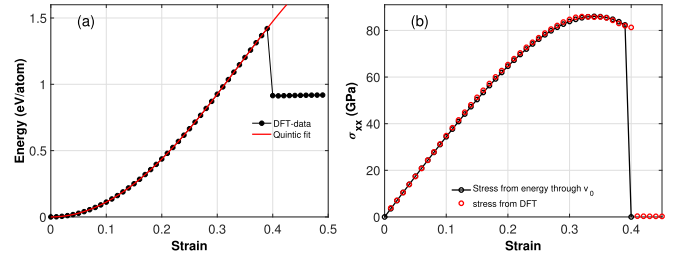


FIG. 4. (a) Potential energy per atom as a function of macroscopic strain in bulk SiC for loading along the [100] direction. (b) Stress-strain curve obtained from DFT-given energy-strain data using v_0 is shown in black. It is compared with the DFT-given stress-strain data shown in red.

as

$$\sigma_{\text{atomistic}} = \beta_1\epsilon_{xx} + \beta_2\epsilon_{xx}^2 + \beta_3\epsilon_{xx}^3 + \beta_4\epsilon_{xx}^4. \quad (7)$$

By construction $\sigma_{\text{atomistic}}$ yields the same stress-strain relation for a bulk as that of σ_{xx} (derived from energy through Eq. 6), and the equality $\sigma_{xx} = \sigma_{\text{atomistic}}$ holds for any value of ϵ_{xx} provided that each of the following relations is satisfied: $\beta_1 = 2C_2v_0$, $\beta_2 = 3C_3v_0$, $\beta_3 = 4C_4v_0$, and $\beta_4 = 5C_5v_0$. In other words the parameter v_0 can be understood as a scaling factor between the stress-strain and energy-strain polynomials:

$$v_0 = \frac{\beta_1\epsilon_{xx} + \beta_2\epsilon_{xx}^2 + \beta_3\epsilon_{xx}^3 + \beta_4\epsilon_{xx}^4}{2C_2\epsilon_{xx} + 3C_3\epsilon_{xx}^2 + 4C_4\epsilon_{xx}^3 + 5C_5\epsilon_{xx}^4}, \quad (8)$$

such that one needs to find out the scaling of the energy-strain curve that matches with the stress-strain curve. The scaling emerges from the existence of one-to-one mapping between stress and energy at every deformation/strain state of the solid [63]. Therefore, in situations where $\sigma_{\text{atomistic}}$ is not accurately obtainable from atomistic data (such as in NWs), the energy-strain data can be employed to predict σ_{xx} with the parameter v_0 known *a priori* from a bulk simulation.

Following the above procedure, we compute v_0 from the DFT-generated energy- and stress-strain data for bulk SiC and use it for NWs. Fitting Eq. (7) to the DFT-generated stress-strain data shown in Fig. 1 and Eq. (5) to the corresponding DFT-generated energy-strain data presented in Fig. 4(a), we obtain the fitting parameters as $\beta_1 = 352.2807$, $\beta_2 = -58.9595$, $\beta_3 = -65.1047$, $\beta_4 = -1824.1879$, $C_2 = 11.400671$, $C_3 = -1.272050$, $C_4 = -1.053475$, and $C_5 = -23.614083$. The R^2 measure of the goodness of the fit was found to be >0.9996 for each of the parameters. The parameters yield $v_0 = 15.45 \text{ \AA}^3$ which satisfies each of the following relations: $\beta_1 = 2C_2v_0$, $\beta_2 = 3C_3v_0$, $\beta_3 = 4C_4v_0$, and $\beta_4 = 5C_5v_0$ with relative errors of $9.6 \times 10^{-6}\%$, $2.96 \times 10^{-5}\%$, $8.44 \times 10^{-5}\%$, and $6.44 \times 10^{-7}\%$, respectively. The relative errors are calculated by using

$(\beta_1 - 2C_2v_0)/\beta_1$, $(\beta_2 - 3C_3v_0)/\beta_2$, $(\beta_3 - 4C_4v_0)/\beta_3$, $(\beta_4 - 5C_5v_0)/\beta_4$, respectively. The negligible relative errors and excellent goodness of the fit are a direct consequence of the one-to-one mapping between stress and energy in the solid. Moreover, we obtain the same value of $v_0 = 15.45$ using the MD-generated stress-strain and energy-strain data.

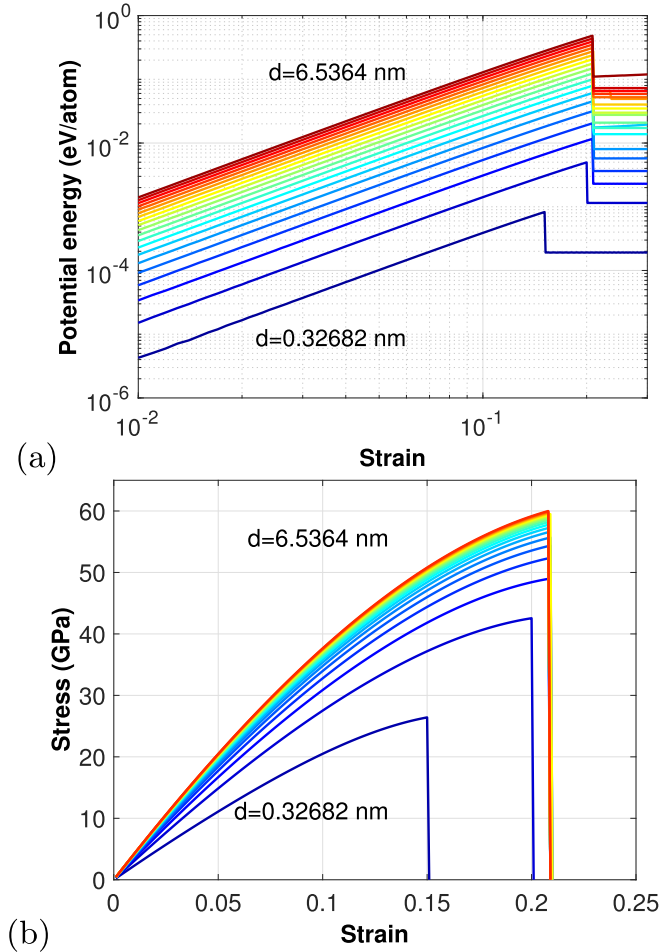


FIG. 5. (a) Potential-energy density relative to the equilibrium as a function of macroscopic strain for 20 nanowires with diameters ranging from 0.32 to 6.53 nm in a log-log plot. (b) Stress-strain curves for the same set of nanowires derived from the energy-strain data. Colors from blue to red represent the diameter cases going from 0.32 to 6.53 nm.

The consistency between the DFT- and MD-predicted values of v_0 indicates the accuracy of the force field fitting. It is noteworthy that the deviation of stress-strain response between MD and DFT in the nonlinear regime of mechanical deformation (as shown in Fig. 1) does not influence the values of v_0 obtained from MD and DFT—this is for the reason that v_0 is a strain-independent constant quantity. It should however be noted that v_0 can vary with temperature as the mapping between stress and energy is temperature dependent, although its effect in brittle solids can be deemed negligible. In Fig. 4(a), the DFT-generated energy-strain data is shown, and in Fig. 4(b) the DFT-generated stress-strain data are compared with the stress-strain curve obtained from energy-strain data through using the effective atomic volume v_0 .

B. Diameter-dependent mechanical behavior

Applying the aforementioned scheme, we determine the uniaxial stress-strain response for 20 nanowires of different diameter from their energy-strain data as illustrated in Fig. 5.

Strain-dependent energy and stress response of the nanowires reveal a number of qualitative trends: (a) The energy density and stress increase nonlinearly with increasing diameter; (b) the higher is the diameter, the stronger, stiffer, and tougher are the nanowire; (c) for sufficiently larger diameters the mechanical properties become diameter independent; (d) the largest diameter considered in this paper has a substantially different mechanical response compared to the bulk; and (e) strength, toughness, and fracture strain follow a different diameter-dependent behavior. Strength is calculated as the maximum of the stress-strain curve: $\sigma_{\max} = \max\{\sigma(\epsilon)\}$; toughness by integrating the area under the stress-strain curve: $\Pi_c = \int_0^{\epsilon_f} \sigma d\epsilon$; and fracture strain as the maximum strain at the onset of fracture: $\epsilon_f = \max\{\epsilon\}$. Stiffness or the Young's modulus is calculated by taking the first-order derivative of the total energy with respect to applied strain,

$$Y = \frac{1}{v_0} \left(\frac{dU}{d\epsilon} \right) \Big|_{\epsilon=0}. \quad (9)$$

To develop a quantitative understanding of the diameter-dependent properties of the nanowires, we plot stiffness, strength, toughness, and fracture strain as a function of diameter as depicted in Fig. 6.

Due to high computational demand in exploring the fracture of a nanowire using DFT, we limit our validation effort to Y for a few smaller diameter nanowires using DFT-GGA calculations. As illustrated in Fig. 6(a), DFT and MD results exhibit consistent behavior on stiffness for all five nanowires—their stiffnesses agree within 1%, and both DFT and MD results show a clear nonlinear trend of higher stiffnesses with increasing diameter. This highlights its reliability for use in situations where DFT is inapplicable due to large computational demand.

To extract the mathematical expressions describing the diameter-dependent mechanical behavior of SiC NWs, we fit the following function (to each of the properties as shown in Fig. 6):

$$\Xi = \Xi(\infty) + \alpha d^n, \quad (10)$$

where $\Xi \in \{\sigma_{\max}, Y, \Pi_c, \epsilon_f\}$ is a diameter-dependent property, Y is the first-order elastic modulus or the Young's modulus, $\Xi(\infty)$ is the value of the property for nanowires with large diameter as $d \rightarrow \infty$, α is a fitting parameter denoting the intensity of the diameter-dependent variation, and n is the exponent indicating how strong is the effect of diameter on that property. The values of the fitting parameters are tabulated in Table I. They exhibit several important characteristics of the mechanical behavior in nanowires: (a) $\Xi(\infty)$ does not approach the value of bulk SiC; (b) diameter-dependent variation does not exactly follow the surface-area-to-volume ratio, which varies as $1/d$; in other words, neither of the exponents is -1 and $\alpha \neq 1$; (c) the existence of a nonzero value for the quantity $\chi = \Xi_{\text{bulk}} - \Xi(\infty)$ suggests the existence of mechanistic effects that are present only in the nanowires (at least, up to $d = 6$ nm) but not in the bulk; and (d) stiffness, strength, toughness, and fracture strain differ in terms of their sensitivity to diameter. For example, compared to bulk SiC, the NW of $d = 2$ nm exhibits a 10% reduction in stiffness, a 14% reduction in strength, a 27% reduction in toughness, and a 12% reduction in fracture strain. The objective of this

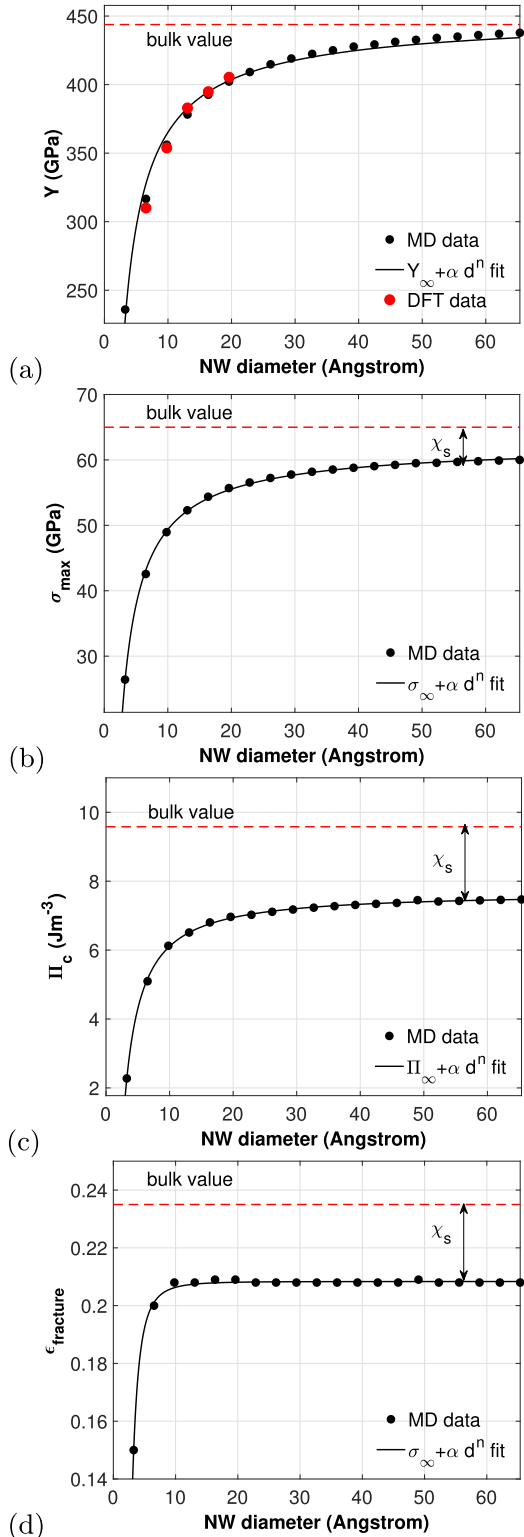


FIG. 6. Diameter-dependent (a) Young’s modulus (Y), (a) ideal strength (σ_{\max}), (b) toughness (Π_c) and (c) fracture-strain (ϵ_f) variation in [111] 3C-SiC nanowires. The horizontal dashed lines indicate the corresponding value of that property in bulk SiC along the [111] direction. The fitting parameters and bulk values are reported in Table I.

paper is to explain these characteristics and investigate their atomistic origins.

TABLE I. Fitting parameters describing the diameter-dependent elastic moduli, strength, toughness, and fracture strain in the 3C-SiC [111] nanowire. The goodness of fit is computed using the R^2 measure and given below. The units of Y , σ_{\max} , and Π_c are gigapascals, gigapascals, and J m^{-3} , respectively, and ϵ_f is dimensionless.

Property					Fit accuracy
Ξ_i	Ξ_{bulk}	$\Xi(\infty)$	α	n	R^2
Y_1	445.0	443.0	-607.35	-0.845	0.9991
σ_{\max}	65.0	62.63	-106.01	-0.902	0.9999
Π_c	9.58	7.66	-20.17	-1.112	0.9999
ϵ_f	0.235	0.208	-2.058	-3.0	0.9993

C. Atomistic origin of the diameter-dependent properties

The presence of a surface can affect mechanical properties: (a) by changing the energy density in the nanowire and (b) by altering the distribution of atomic stress. Here, we show that the former governs the elastic state of the nanowire, particularly, in the linear regime forming the basis for softening and stiffening behavior of the nanowire and the latter governs extreme mechanical properties, such as toughness, strength, and fracture strain that describe the condition for fracture.

Although for a nanowire, failure is assumed to originate from the surface—it remains unknown if the location and condition for crack initiation and its propagation path can be predicted to circumvent its ramifications. Although the surface atoms are the highest potential-energy atoms in a NW due to their missing neighbors, they are the least stressed atoms because of the traction-free condition on the surface. Also, they can accommodate larger displacements due to softening of the bonds. With increasing d , the number of surface atoms becomes insignificant compared to the core so that the behavior of the nanowires is dominated by the core—and a generic trend can be approximated using the surface-area-to-volume ratio that varies as $1/d$. Although our MD data support an inverse diameter dependence for both toughness and strength, there is a sizable deviation from this simpler approximation. We examine the energy density and atomic stress to determine the underlying atomistic basis behind the inverse d dependence of toughness and strength in the NWs.

1. Diameter-dependent energy density

Plotting the average potential-energy density (eV/atom) u as a function of diameter d , we find $u(d) - u_{\infty} = 3.0209d^{-0.6954}$ which manifests a slower decrease in u compared to what is obtained from d^{-1} approximation at the undeformed state of the nanowires (see Fig. 7). This dependence is obtained by computing u for different nanowires and fitting them to $u(d) - u_{\infty} = \alpha d^n$ with $R^2 = 0.9993$ as a goodness of fit for the fitted parameters.

We attribute the slower decay in stiffness to arise from the atoms at the intersection of the core and surface in the nanowires. With increasing diameter, the energy density u at the surface increases as d^1 , at the core as d^2 , and at the surface-core intersection between d^1 and d^2 . Thus their combined effect on energy density is $d^{-0.69}$, and it is substantially

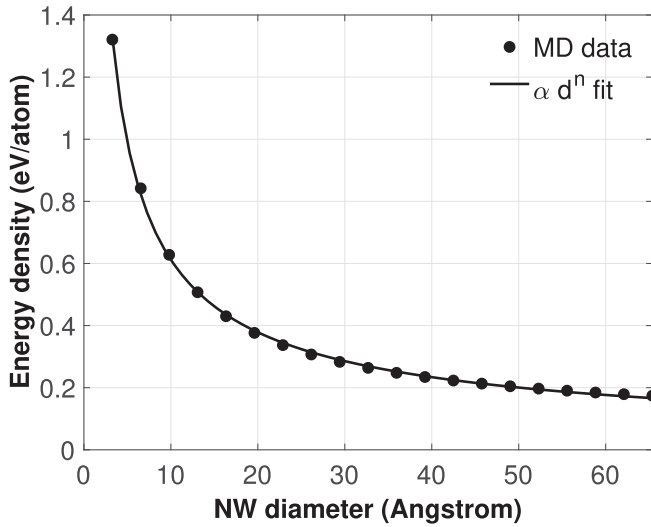


FIG. 7. Potential-energy density at the equilibrium as a function of nanowire diameter relative to the potential-energy density in bulk SiC.

smaller than what we would get from the surface-area-to-volume ratio. Nonetheless this $d^{-0.69}$ dependence of potential-energy density at the equilibrium does not explain fully the atomistic basis for the $d^{-0.9}$ dependence of strength. We propose two mechanisms behind this. First, $d^{-0.845}$ -dependent stiffness variation in NWs indicates a higher stress level in wider nanowires for a given amount of applied strain.

Although at the equilibrium the energy density is higher in thinner nanowires due to a higher ratio of surface vs core atoms, under the application of axial force, the change in energy density is smaller in thinner nanowires due to the possibility of higher deformational energy accommodation by the surface atoms. As a result, the larger is the diameter, the stiffer is the nanowire, and the higher is the change in energy density. This picture is consistent with Fig. 6(a) that shows higher stiffness with increasing diameter. Second, the presence of stress heterogeneity in the nanowire that can enhance the average stress level with increasing deformation and play a critical role in governing the condition for fracture as elucidated in the following section.

2. Heterogeneity in atomic stress

To determine the diameter-dependent trends in σ_{\max} , Π_c , and ϵ_f and the observation that $\chi \neq 0$, we calculate atomic stress in the nanowires using the virial scheme [68,69] as implemented in LAMMPS. The atomic stresses obtained from MD are in the units of pressure times volume that we convert to stress by dividing the quantity with the effective atomic volume v_0 . As illustrated in Fig. 8, the normal atomic-stress $\sigma_{xx}^{\text{atomic}}$ is highly heterogeneous in the nanowire.

It is also evident that the pattern of the heterogeneous stress field is diameter dependent for smaller NWs, but the pattern saturates in wider nanowires. The maximum stress occurs at the center in ultrathin NWs (of diameters 0.32–0.65 nm), whereas it appears near the edge in larger NWs at their six corners. For the nanowires of higher diameters,

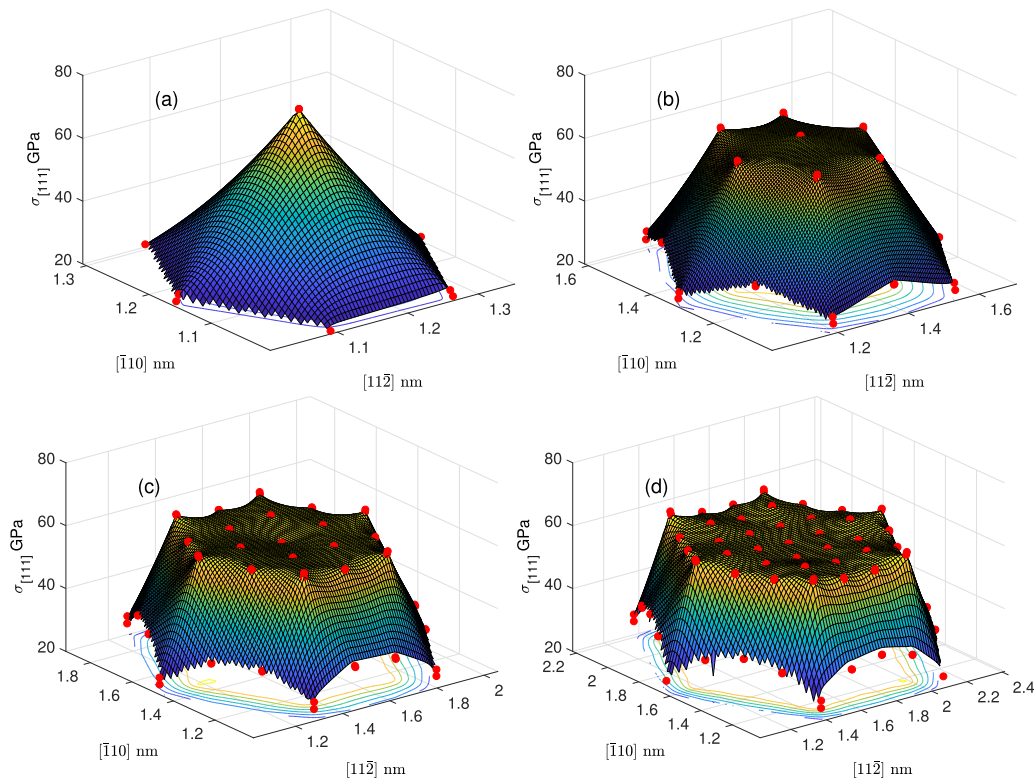


FIG. 8. (a) Heterogeneous atomic-stress $\sigma_{xx}^{\text{atomic}}$ at 20% macroscopic strain in nanowires of (a) 0.32 nm, (b) 0.65 nm, (c) 0.98 nm, and (d) 1.30 nm. The stress range used for all the plots is 20–70 GPa. The color in the plot corresponds to the value of stress shown on the vertical axis.

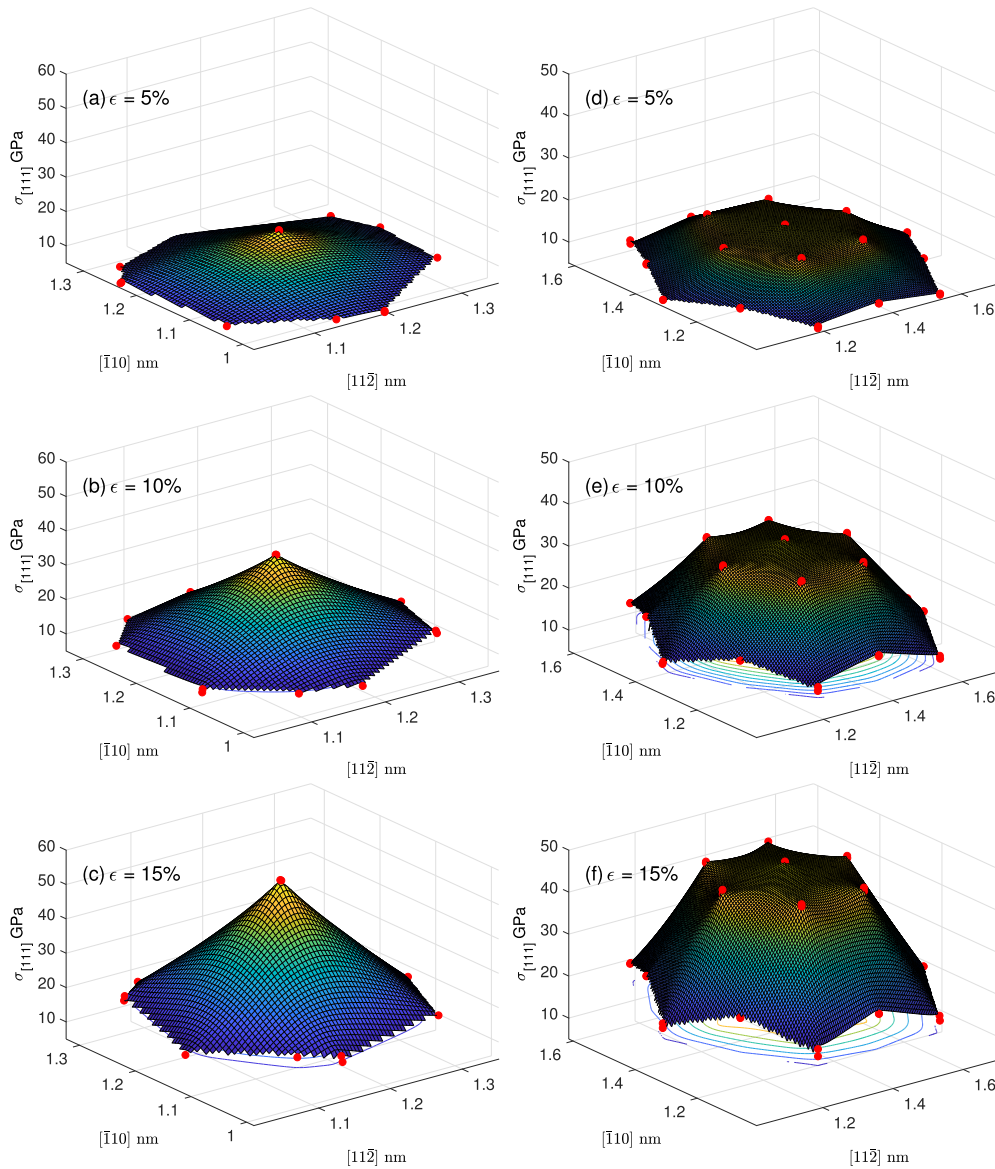


FIG. 9. Evolution of diameter-dependent heterogeneity in atomic-stress $\sigma_{[111]}^{\text{atomic}}$ in (a)–(c) for 0.32-nm NW and in (d)–(f) for 0.65-nm NW. The color in the plot corresponds to the value of stress shown on the vertical axis.

the stress field exhibits three distinct regimes: (i) The highest stress appears at the intersection between the surface and the core with a larger concentration at six corners, (ii) the lowest stress appears on the surface, and (iii) the core exhibits uniform stress distribution. The stress intensity slowly decreases radially inward and rapidly outward from the six corners. Consequently, the surface atoms remain as the least stressed atoms in the nanowire regardless of the loading intensity in the nanowire or its diameter.

The heterogeneity in atomic stress does not affect the elastic behavior in the linear regime because in the undeformed state the stress field is mostly homogeneous in all the nanowires. Their mechanical behavior is governed by the diameter-dependent energy density that is described in the previous section. With increasing strain, the stress field becomes heterogeneous, and the intensity of heterogeneity increases with applied strain. As a result, the higher is the

diameter, the higher is the stress heterogeneity as exhibited in Fig. 9 for two thin nanowires at three different strain states.

The presence of stress heterogeneity makes the nanowires fail earlier compared to the bulk (as seen before quantitatively in Fig. 6). Although stiffness of wider NWs approaches the bulk value, their toughness, strength, and fracture strain do not approach the same due to the continued presence of stress heterogeneity in wider nanowires at higher deformation. It can thus be concluded that no matter how large is the diameter of the nanowire due to the presence of the surface, there is a stress localization or stress heterogeneity present in the nanowire, and it appears near the surface at higher deformation in larger nanowires. As the loading is increased, the intensity of stress heterogeneity increases. As a result, even a very large diameter nanowire would fail earlier than the bulk because of the appearance or activation of this stress heterogeneity at higher deformation.

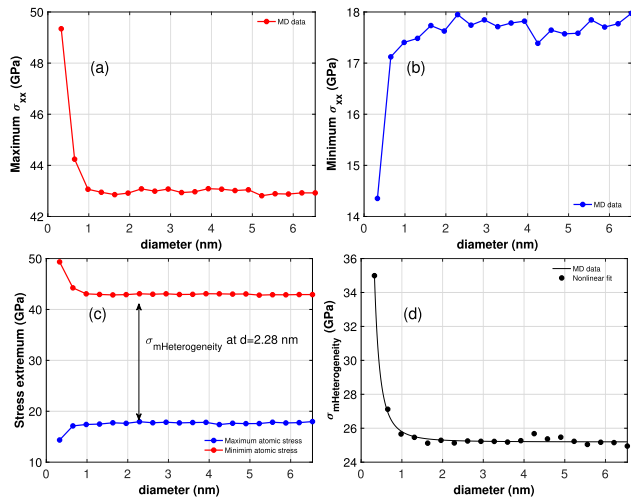


FIG. 10. (a) Diameter-dependent maximum normal atomic-stress $\sigma_{xx}^{\text{atomic}}$ and (b) diameter-dependent minimum normal atomic-stress $\sigma_{xx}^{\text{atomic}}$ at 15% strain. (c) Comparison of the maximum and minimum stresses and observation of saturation in stress heterogeneity indicated by the vertical line. (d) Diameter-dependent maximum stress-heterogeneity $\sigma_{\text{mHeterogeneity}}$. The stress extremum is calculated with an error bar of 0.1 GPa denoting the variation in values among the six corner sites where it is the maximum.

Furthermore, for a given nanowire there is a sizable difference between the maximum and the minimum normal atomic stresses in a section, and this difference increases with diameter and saturates at higher diameters. To determine their trend, we define the difference as the *maximum stress heterogeneity* in the nanowire, and denote it as

$$\sigma_{\text{mHeterogeneity}} = \max \sigma_{xx}^{\text{atomic}} - \min \sigma_{xx}^{\text{atomic}}, \quad (11)$$

where, $\max \sigma_{xx}^{\text{atomic}}$ and $\min \sigma_{xx}^{\text{atomic}}$ are the maximum and minimum atomic stresses in the nanowire and plot their dependence on diameter at a given strain in Fig. 10. At 20% strain $\sigma_{\text{mHeterogeneity}}$ becomes diameter independent beyond 2.0 nm, and its value saturates at around 25.19 GPa. The diameter-dependent behavior at this loading state is well fitted by $25.19 + 0.6093d^{-2.48}$ with a R^2 measure of 0.9913. Due to the large magnitude of $\max \sigma_{xx}^{\text{atomic}}$ for the thinnest nanowire, it fails upon reaching this loading, and the second thinnest nanowire fails next. The remaining nanowires of $d > 1$ nm continue developing stress heterogeneity with continued loading and eventually all of them fail at the same strain level as depicted in Fig. 6. Due to saturation of stress heterogeneity in these nanowires diameter-dependent behavior of ϵ_f exhibits rapid saturation with diameter. Therefore, the presence of saturated stress heterogeneity in wider nanowires forms the basis for the lower values of fracture strain in wide nanowires (with $d \rightarrow \infty$) and that of the bulk SiC, in other words $\sigma_{\text{mHeterogeneity}}$ explains the reason for $\epsilon_f^{\text{bulk}} - \epsilon_f^{\text{NW}} \neq 0$ (as shown in Fig. 6).

Although diameter-dependent fracture-strain $\epsilon_f(d)$ closely follows the trend in stress-heterogeneity, diameter-dependent strength $\sigma_{\text{max}}(d)$ and toughness $\Pi_c(d)$ respond to stress heterogeneity differently: They vary much slower with changes in diameter compared to ϵ_f . This is likely for the following reasons. First, ϵ_f is governed by a condition wherein one bond

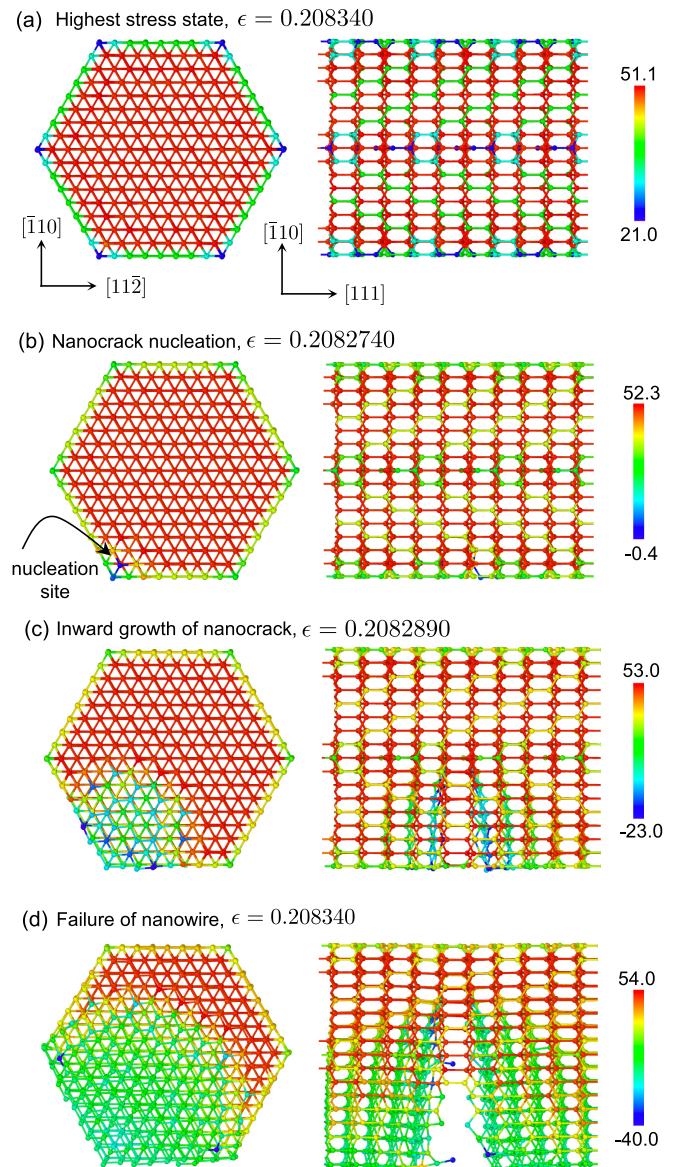


FIG. 11. Stress-heterogeneity-induced nanocrack nucleation and its inward evolution in a 2.61-nm nanowire. The units of stress are gigapascals.

has to reach the maximum bond force to initiate fracture. There are six columns of atoms aligned along the loading direction in [111]-SiC NWs, and all of them deform identically in nanowires with $d > 1$ nm owing to identical stress heterogeneity state in them. On the other hand, in thinner NWs $d < 1$ nm, stress heterogeneity is dominated in a single column of atoms located at the core. Therefore, they fail quickly due to a higher stress gradient across the nanowire. Although fracture strain is directly related to the strain at the bond level, the measure of strength involves the average response of the nanowire and therefore involves contributions of all atoms in a cross section. Despite the saturation of the maximum stress heterogeneity at a given strain state, there is a substantial difference among the NWs in terms of their average stress state. The difference arises from combined effects of diameter-dependent stiffness and higher-order elastic

moduli. Thus, heterogeneity in energy density correlates with that in stress in governing diameter-dependent strength in nanowires. Similarly, diameter-dependent toughness (which integrates the stress-strain response of the solid over the entire deformation) is modulated by the combined effects of heterogeneities in energy density and atomic stress. As a consequence, there is a significant effect of $\sigma_{\text{mHeterogeneity}}$ on $\Pi_c^{\text{bulk}} - \Pi_c^{\text{NW}}$, and its value is as large as 23% of bulk value in SiC.

In addition to affecting the values of toughness and strength, stress heterogeneity has a critical implication in the nanowire: It localizes crack nucleation. As depicted in Fig. 11, the location of highest stress heterogeneity precisely identifies the breeding site for crack nucleation, and the gradient in stress heterogeneity dictates the immediate direction of crack growth. It is noticeable that at the highest stress state ($\epsilon = 0.2082740$), one of the six corners of the NW is randomly picked by the nanowire as a breeding zone for nanocrack nucleation. Continued loading makes the incipient nanocrack invade the nanowire cross section radially inward causing material separation to take place in a brittle manner. The entire crack nucleation and separation process completes within a strain window of only 1.0×10^{-4} , exhibiting rapid invasion of the nanowire cross section by the nucleated crack and producing a brittle character for the failure process. Also, during crack propagation, the maximum atomic stress in the NW continues to increase its intensity at the propagating crack front leaving a compressive trail behind. As soon as one of the six nucleation sites becomes activate, the remain sites cease to act as a nucleating site. We observe similar processes in failure for all the NWs of $d > 1$ nm wherein nanocracks evolve from the intersection of the core and surface atoms where the stress heterogeneity is the maximum. The NWs of the $d < 1$ -nm crack, however, nucleates at the core and propagates radially outward.

The above observation and analysis suggest that degradation in extreme mechanical properties of the SiC NW is

substantially affected by heterogeneity in stress and energy density, irrespective of its diameter. Due to pronounced stress heterogeneity at the six corners of the nanowire in wider nanowires, localization on nanocrack nucleation always occurs at one of its six corners, and it ruptures the nearest bond aligned normal to the surface due to a steep gradient in stress heterogeneity. The propagation is then followed uniformly radially toward to rest of the nanowire cross section. This prediction is well manifested by the crack nucleation and propagation events in a wider nanowire as shown in Fig. 11.

IV. CONCLUDING REMARKS

To conclude, we have shown that heterogeneity in atomic stress plays a critical role in governing diameter-dependent strength and toughness in SiC nanowires. As the scale of materials shrinks to the nanometer scale, the surface potential effects extend beyond the surface layers and into the core-inducing diameter dependence into stiffness, strength, and toughness of NWs. We propose that the nonuniformity in potential energies across the cross section of the nanowire penetrates into the core for smaller nanowires and configures heterogeneity in atomic stress. For smaller diameter nanowires the surface potential leads to substantial stress heterogeneity making them more susceptible to fracture when subjected to axial loading. For wider nanowires, the stress heterogeneity saturates at higher deformation and constitutes the reduction in strength and toughness compared to its bulk counterpart. Our investigation was carried out with an energy-based framework that eliminated the need for using macroscopic geometric information (such as volume or diameter) and yet produced accurate estimation of elastic and strength properties of SiC that are consistent with the DFT results. We anticipate that the approach and results presented herein will find important applications in designing NWs or nanowire-based composites.

-
- [1] Y. Kondo, Q. Ru, and K. Takayanagi, *Phys. Rev. Lett.* **82**, 751 (1999).
- [2] H. S. Park, *Nano Lett.* **6**, 958 (2006).
- [3] W. Liang, M. Zhou, and F. Ke, *Nano Lett.* **5**, 2039 (2005).
- [4] H. S. Park, K. Gall, and J. A. Zimmerman, *Phys. Rev. Lett.* **95**, 255504 (2005).
- [5] W. Tao, P. Cao, and H. S. Park, *Nano Lett.* **18**, 1296 (2018).
- [6] G. Cheng, S. Yin, T.-H. Chang, G. Richter, H. Gao, and Y. Zhu, *Phys. Rev. Lett.* **119**, 256101 (2017).
- [7] Z. Yan and L. Jiang, *Nanomaterials* **7**, 27 (2017).
- [8] D. Söpu, A. Foroughi, M. Stoica, and J. Eckert, *Nano Lett.* **16**, 4467 (2016).
- [9] W. Zhang, T. Wang, and X. Chen, *J. Appl. Phys.* **103**, 123527 (2008).
- [10] L. Lühns, B. Zandersons, N. Huber, and J. Weissmüller, *Nano Lett.* **17**, 6258 (2017).
- [11] G. Y. Jing, H. L. Duan, X. M. Sun, Z. S. Zhang, J. Xu, Y. D. Li, J. X. Wang, and D. P. Yu, *Phys. Rev. B* **73**, 235409 (2006).
- [12] M. E. Gurtin and A. I. Murdoch, *Int. J. Solids Struct.* **14**, 431 (1978).
- [13] J. R. Smith, *Phys. Rev.* **181**, 522 (1969).
- [14] N. Lang and W. Kohn, *Phys. Rev. B* **1**, 4555 (1970).
- [15] H. Hoppe, T. DeRose, T. Duchamp, J. McDonald, and W. Stuetzle, *Surface Reconstruction from Unorganized Points* (ACM, New York, 1992), Vol. 26.
- [16] K. L. Johnson, K. Kendall, and A. Roberts, *Proc. R. Soc. London Ser. A* **324**, 301 (1971).
- [17] A. W. Adamson and A. P. Gast, *Physical Chemistry of Surfaces* (Interscience publishers, New York, 1967).
- [18] H. Liang, M. Upmanyu, and H. Huang, *Phys. Rev. B* **71**, 241403 (2005).
- [19] N. Mameka, J. Markmann, and J. Weissmüller, *Nat. Commun.* **8**, 1976 (2017).
- [20] S. Parida, D. Kramer, C. A. Volkert, H. Rösner, J. Erlebacher, and J. Weissmüller, *Phys. Rev. Lett.* **97**, 035504 (2006).
- [21] H.-J. Jin, X.-L. Wang, S. Parida, K. Wang, M. Seo, and J. Weissmüller, *Nano Lett.* **10**, 187 (2009).
- [22] B.-N. D. Ngô, A. Stukowski, N. Mameka, J. Markmann, K. Albe, and J. Weissmüller, *Acta Mater.* **93**, 144 (2015).

- [23] Y. Zhu, Q. Qin, F. Xu, F. Fan, Y. Ding, T. Zhang, B. J. Wiley, and Z. L. Wang, *Phys. Rev. B* **85**, 045443 (2012).
- [24] G. Richter, K. Hillerich, D. S. Gianola, R. Monig, O. Kraft, and C. A. Volkert, *Nano Lett.* **9**, 3048 (2009).
- [25] J.-H. Seo, Y. Yoo, N.-Y. Park, S.-W. Yoon, H. Lee, S. Han, S.-W. Lee, T.-Y. Seong, S.-C. Lee, K.-B. Lee *et al.*, *Nano Lett.* **11**, 3499 (2011).
- [26] S. Vlassov, B. Polyakov, L. M. Dorogin, M. Antsov, M. Mets, M. Umalas, R. Saar, R. Löhmus, and I. Kink, *Mater. Chem. Phys.* **143**, 1026 (2014).
- [27] J. Oliveira, J. Morbec, and R. Miwa, *J. Appl. Phys.* **121**, 104302 (2017).
- [28] G. Cheng, T.-H. Chang, Q. Qin, H. Huang, and Y. Zhu, *Nano Lett.* **14**, 754 (2014).
- [29] T.-Y. Zhang, M. Luo, and W. K. Chan, *J. Appl. Phys.* **103**, 104308 (2008).
- [30] P. Hu, S. Dong, X. Zhang, K. Gui, G. Chen, and Z. Hu, *Sci. Rep.* **7**, 3011 (2017).
- [31] S. Wang, Z. Shan, and H. Huang, *Adv. Sci.* **4**, 1600332 (2017).
- [32] Y. Zhu, *Appl. Mech. Rev.* **69**, 010802 (2017).
- [33] L. Su, H. Wang, M. Niu, X. Fan, M. Ma, Z. Shi, and S.-W. Guo, *ACS Nano* **12**, 3103 (2018).
- [34] B. Sun, Y. Sun, and C. Wang, *Small* **14**, 1703391 (2018).
- [35] H.-P. Phan, K. M. Dowling, T. K. Nguyen, T. Dinh, D. G. Senesky, T. Namazu, D. V. Dao, and N.-T. Nguyen, *Mater. Des.* **156**, 16 (2018).
- [36] Y. Yao, X. Zhu, X. Zeng, R. Sun, J.-B. Xu, and C.-P. Wong, *ACS Appl. Mater. Interfaces* **10**, 9669 (2018).
- [37] J. Fan and P. K. Chu, *Silicon Carbide Nanostructures: Fabrication, Structure, and Properties* (Springer, Berlin, 2014).
- [38] B. Yan, G. Zhou, W. Duan, J. Wu, and B.-L. Gu, *Appl. Phys. Lett.* **89**, 023104 (2006).
- [39] J. L. Cuevas, F. De Santiago, J. Ramírez, A. Trejo, Á. Miranda, L. A. Pérez, and M. Cruz-Irisson, *Comput. Mater. Sci.* **142**, 268 (2018).
- [40] H.-K. Seong, H.-J. Choi, S.-K. Lee, J.-I. Lee, and D.-J. Choi, *Appl. Phys. Lett.* **85**, 1256 (2004).
- [41] P. W. Leu, A. Svizhenko, and K. Cho, *Phys. Rev. B* **77**, 235305 (2008).
- [42] M. A. Makeev, D. Srivastava, and M. Menon, *Phys. Rev. B* **74**, 165303 (2006).
- [43] Z. Wang, M. Zhao, T. He, H. Zhang, X. Zhang, Z. Xi, S. Yan, X. Liu, and Y. Xia, *J. Phys. Chem. C* **113**, 12731 (2009).
- [44] P. Hohenberg and W. Kohn, *Phys. Rev.* **136**, B864 (1964).
- [45] D. Sangiovanni, *Acta Mater.* **151**, 11 (2018).
- [46] J. Tersoff, *Phys. Rev. B* **39**, 5566 (1989).
- [47] P. Vashishta, R. K. Kalia, A. Nakano, and J. P. Rino, *J. Appl. Phys.* **101**, 103515 (2007).
- [48] B. Zheng and J. E. Lowther, *Nanoscale* **2**, 1733 (2010).
- [49] F. H. Stillinger and T. A. Weber, *Phys. Rev. B* **31**, 5262 (1985).
- [50] M. Hossain, T. Hao, and B. Silverman, *J. Phys.: Condens. Matter* **30**, 055901 (2018).
- [51] M. Z. Hossain, T. Ahmed, B. Silverman, M. S. Khawaja, J. Calderon, A. Rutten, and S. Tse, *J. Mech. Phys. Solids* **110**, 118 (2018).
- [52] T. Ahmed, A. Proca, T. Hao, and Z. M. Hossain (unpublished).
- [53] *Properties of Silicon Carbide*, edited by G. L. Harris, EMIS Datareviews Series Vol. 13 (INSPEC, London, 1995).
- [54] J. M. Soler, E. Artacho, J. D. Gale, A. García, J. Junquera, P. Ordejón, and D. Sánchez-Portal, *J. Phys.: Condens. Matter* **14**, 2745 (2002).
- [55] N. Troullier and J. L. Martins, *Phys. Rev. B* **43**, 1993 (1991).
- [56] J. P. Perdew, K. Burke, and M. Ernzerhof, *Phys. Rev. Lett.* **77**, 3865 (1996).
- [57] O. Auciello, J. Birrell, J. A. Carlisle, J. E. Gerbi, X. Xiao, B. Peng, and H. D. Espinosa, *J. Phys.: Condens. Matter* **16**, R539 (2004).
- [58] S. Plimpton, *J. Comput. Phys.* **117**, 1 (1995).
- [59] D. P. Landau and K. Binder, *A Guide to Monte Carlo Simulations in Statistical Physics* (Cambridge University Press, Cambridge, UK, 2014).
- [60] S. Nosé, *J. Chem. Phys.* **81**, 511 (1984).
- [61] H. C. Andersen, *J. Chem. Phys.* **72**, 2384 (1980).
- [62] S. Nosé and M. Klein, *Mol. Phys.* **50**, 1055 (1983).
- [63] A. E. H. Love, *A Treatise on the Mathematical Theory of Elasticity* (Cambridge University Press, Cambridge, UK, 2013).
- [64] R. A. Toupin, *Arch. Ration. Mech. Anal.* **18**, 83 (1965).
- [65] C. O. Horgan and J. K. Knowles, in *Advances in Applied Mechanics*, edited by J. W. Hutchinson and T. Y. Wu (Academic, San Diego, 1983), Vol. 23, pp. 179–269.
- [66] C. Horgan, *Appl. Mech. Rev.* **49**, S101 (1996).
- [67] J. F. Nye, *Physical Properties of Crystals* (Oxford University Press, Oxford, 1985).
- [68] O. H. Nielsen and R. M. Martin, *Phys. Rev. Lett.* **50**, 697 (1983).
- [69] O. H. Nielsen and R. M. Martin, *Phys. Rev. B* **32**, 3780 (1985).